ELSEVIER

Biochimica et Biophysica Acta 1193 (1994) 330–344

BBA Biochimica et Biophysica Acta

Changes in Friend murine erythroleukaemia cell membranes during induced differentiation determined by electrorotation

Xiao-Bo Wang [a], Ying Huang [a,b], Peter R.C. Gascoyne [a,*], Frederick F. Becker [a], Ralph Hölzel [c], Ronald Pethig [b]

[a] *University of Texas M.D. Anderson Cancer Center, 1515 Holcombe Boulevard, Houston, TX 77030, USA*
[b] *Institute of Molecular and Biomolecular Electronics, University of Wales, Dean Street, Bangor, Gwynedd LL57 1UT, UK*
[c] *Institut für Biophysik der Freien Universität Berlin, Thielallee 63, 14195 Berlin, Germany*

Received 21 December 1993

Abstract

We used electrorotation measurements to investigate alterations in the plasma membranes of DS19 murine erythroleukaemia cells that accompanied erythropoietic differentiation induced by hexamethylene bisacetamide (HMBA). Following 3 days of HMBA treatment, the mean cell membrane specific capacitance determined from electrorotation spectra of individual, viable cells at physiological tonicity (300 mosmol/kg) fell from 1.74 to 1.53 $\mu F/cm^2$, in agreement with trends observed earlier by dielectrophoretic measurements on bulk cell populations. Scanning and transmission electron microscopy revealed that the relatively high values found for cell membrane capacitance ($> 1\ \mu F/cm^2$) reflected the large area of plasma membrane associated with complex surface morphology including numerous microvilli. Furthermore, it demonstrated that the fall in membrane capacitance during HMBA treatment correlated with a reduction in the density of these complex surface features. Differences in the mechanical characteristics of the cell membranes of untreated and treated cells were then examined by exposing cells to osmotic stress. The intricacy of membrane morphology intensified with increasing osmolality of the suspending medium and this was reflected in higher specific capacitance values. When the osmolality was increased from 210 to 450 mosmol/kg, the mean membrane capacitance of untreated DS19 cells changed from 1.58 to 2.05 $\mu F/cm^2$ while that for HMBA-treated cells changed from 1.47 to 1.72 $\mu F/cm^2$, a significantly smaller response. This demonstrated that cells exposed to 72 h of differentiation treatment had an enhanced mechanical resilience as compared with their untreated counterparts, evidencing the early stages of the development of the membrane skeleton which becomes fully developed in mature erythrocytes. Our findings demonstrate the value of electrorotation measurements as a method for the non-invasive characterisation of viable leukaemic cells and their responses to stimuli and show that the membrane capacitance values so derived reflect membrane morphology.

Key words: Electrorotation; Dielectrophoresis; Membrane capacitance; Cell dielectric property; Cell differentiation; Leukemia; Cell surface morphology

1. Introduction

Recently there has been a growing interest in the utilisation of AC electric field-induced kinetic effects such as dielectrophoresis (DEP) and electrorotation (ROT) [1–10] for the electrical characterisation and manipulation of biological cells. When a cell, suspended in a medium of different dielectric properties, is subjected to an electric field, charges are induced at the interfaces resulting in a dipole moment along the direction of the applied field. If the field is non-uniform, the electrostatic forces acting on opposite ends of the dipole are different and the net dielectrophoretic force that results can induce translational movement of the cell [1,2]. Unlike electrophoresis, which operates with a DC field, DEP is also effective with AC fields because the dipole moment induced on

---

[*] Corresponding author. Fax: +1 (713) 7925940.

SSDI 0005-2736(94)00080-I

the cell reverses with applied field reversals, thereby maintaining a constant direction of the DEP force.

When a cell is placed into a rotating electric field, a dipole moment is induced that rotates synchronously with the applied field but tends to lag behind it at a constant angle [1,7,8]. The electrostatic interaction between the field and this dipole moment causes a torque to be exerted on the cell, resulting in cell electrorotation. The DEP force and ROT torque are closely related [11,12] through the induced dipole moment. The rate and direction of these effects depend strongly on the cell characteristics and frequency of the applied electric field, and the cell dielectric properties can be deduced from these dependencies [2–10].

Through measurement of the variation of the DEP-induced velocity with the suspending medium conductivity [13,14] using computerised image analysis [15], we recently reported that a 30% drop in membrane specific capacitance and a 5-fold decrement in membrane conductivity accompanied the induction of differentiation of DS19 Friend murine erythroleukaemia (MEL) cells. Using the fluid-mosaic model of the membrane [16,17], it was argued that these relatively large changes were mainly accounted for by alterations in membrane morphology rather than by alterations in its composition. To investigate this further, we have attempted to manipulate the morphology of the membranes of DS19 MEL cells by exposing them to different osmotic environments. Previously, the effects of osmotic perturbation on the electrical properties of cultured cells have been investigated by dielectric suspension and ROT techniques [18,19]. These measurements demonstrated that the membrane capacitance of cells depended on osmolality and suggested that membrane distortion occurred. Here we report ROT measurements on DS19 cells as a function of differentiation-inducing treatment by hexamethylene bisacetamide (HMBA) in media ranging from 140 to 450 mosmol/kg, spanning the physiological tonicity of 300 mosmol/kg.

The ROT responses were analysed using the single-shell dielectric model of the cell and this showed that the specific membrane capacitance fell following differentiation treatment, in agreement with our previous DEP studies [13,14]. Both untreated and HMBA-treated cells exhibited increasing membrane capacitance with increasing suspension osmolality. Scanning electron microscopy (SEM) of the plasma membrane surface morphology led us to conclude that the high effective membrane specific capacitances (> 1 $\mu F/cm^2$) mainly resulted from cell surface features that contributed a much larger membrane area than that of a smooth sphere. This concept was introduced by Arnold and Zimmermann's group in attempting to explain the changes in membrane capacitance observed when T and B lymphocytes were subjected to mitotic stimulation [20] and was given further discussion by them in attempting to analyse the response of cell membrane capacitance to changes in cell suspension osmolality [19]. Here, for the first time, we present electrorotation measurements in conjunction with electron microscopic evidence to support this concept. We show that the extent of membrane-rich features on the cell surface was responsive to the cell suspension osmolality and that membrane capacitance values again directly reflected surface morphology. While the mean membrane capacitance of untreated DS19 cells showed a large (30%) increase when the osmolality was changed from 210 to 450 mosmol/kg, HMBA-treated cells showed a significantly lower response (17%). This demonstrates an increased rigidity of HMBA-treated cells which is compatible with the initial stages of the development of the membrane skeleton of MEL cells during the first 72 h of induced differentiation [21–23].

2. Materials and methods

2.1. Cell culture

Cells of Friend murine erythroleukaemia line DS19 were seeded at $1.5 \cdot 10^4$ cells/ml and grown in 35 ml of RPMI 1640 medium supplemented with 10% foetal bovine serum, 1 mM glutamine and 20 mM Hepes buffer in 75-cm^2 vented culture flasks (Costar) at 37°C under a 5% CO_2/95% air atmosphere. Cultures were in the flask for about 72 h at which time cell density had reached about 10^6 cells/ml with at least 98% viability. Cell cycle kinetics were investigated by ethidium bromide staining and flow cytometry to ensure that cells were in log phase at the time of harvest; the cell doubling time was approx. 12 h. In differentiation treatments, 4 mM hexamethylene bisacetamide (HMBA, Sigma) was added during seeding. HMBA-treated cells were cultured in parallel with the untreated samples to ensure identical growth conditions. At harvest, cells were suspended by gently rocking their culture flasks; no centrifugation or other manipulations were required.

Each ROT sample was prepared by diluting 1 part of the suspended culture with 21 parts of appropriate sucrose/dextrose solution (see below), to yield a cell suspension of $5.0 \cdot 10^4$ cells/ml with a nominal medium conductivity of 560 $\mu S/cm$, as measured using a digital conductivity meter (Cole-Parmer Instruments). To achieve the nominal osmolalities of 140, 210, 300, 370 and 450 mosmol/kg, sucrose concentrations of, respectively, 40, 62.5, 85, 100 and 125 mg/ml, plus 3 mg/ml dextrose, were used [24].

Many cell types are known to undergo a dynamic volume change [25–27] when they are suspended in anisotonic media. As a precaution against making measurements during such responses in DS19 cells, we allowed freshly-made suspensions to stand for at least 15 min before ROT measurements were taken. We observed previously that ions leaked across the plasma membrane of DS19 cells when they were suspended in pure sucrose solution, leading to a gradual increase in suspension conductivity [13]. However, at the low cell concentrations and comparatively high suspension conductivity used here, such leakage resulted in a conductivity change of only 1% during the 30 min needed to take an entire ROT spectrum.

2.2. ROT measurements

The ROT chamber, consisting of a 15 mm diameter × 1 mm thick O-ring glued over the electrode substrate, and the polynomial electrode geometry have been described earlier [28]. A polynomial electrode having a tip-tip spacing of 400 μm was convenient for measurements on the DS19 cells, which had a mean diameter of about 12 μm. The electrode was cleaned thoroughly, and soaked overnight, in deionised water to ensure minimal adherence of cells to the electrode substrate. For each experiment, 200 μl of cell suspension was pipetted into the O-ring and a cover slip was gently depressed over its center to form a full, well-sealed chamber. This prevented cells from drifting during the ROT measurements.

After cells had settled for about 2 min, a 50-kHz voltage was applied to the electrodes for 10 s to direct cells into the central region of the electrodes by negative DEP [28,29]. ROT measurements were taken on cells located within 100 μm of the center of the electrode geometry to minimise the influence of DEP-induced lateral cell motion. Also, to minimise dipole–dipole interactions between neighbouring cells, measurements were not taken for those with neighbours less than about three cell diameters away. In this way, each filling of the chamber typically allowed measurements on two to four cells.

The rotating field was established by energising the electrodes with four sinusoidal voltages of 0.9 V (RMS) in phase quadrature, provided by a specially-built signal generator supplied via four 50-Ω coaxial cables terminated with 50-Ω resistors at the electrodes. The cell electrorotational effects were monitored over the frequency range 10 kHz to 100 MHz using a Nikon Diaphot TMD inverted microscope equipped with a Hamamatsu CCD video camera and recorded onto video tape for later measurements of cell ROT rate using a stopwatch. Four separate stopwatch measurements were taken for each ROT experimental point. A statistical analysis of the timing data for all the cells studied showed that the relative measurement error (ROT rate variance divided by the mean) could be described by a Gaussian distribution with zero mean and less than 0.03 variance. Cell sizes were measured using a customised program based on the Optimas (Bioscan) imaging processing system.

2.3. Scanning electron microscopy (SEM)

Untreated and HMBA-treated cells were washed with 125 mM sodium cacodylate buffer (pH 7.3, adjusted to 300 mosmol/kg with NaCl) at 37°C and fixed at this temperature with modified Karnovsky's fixative (pH 7.5) for at least 30 min. The cells were then rinsed three times in 125 mM sodium cacodylate buffer for 5-min periods and post-fixed in 2% OsO_4 in the same buffer for 30 min at room temperature (22°C). After three more rinses in the cacodylate buffer, cells were dehydrated in a graded ethanol series, transferred to Peldri II (Ted Pella) for critical-point dehydration and placed in a vacuum desiccator for 24 h. After sublimation of the fluorocarbon, the cells were mounted onto stubs, sputter-coated in a Hummer VI (Technics, Springfield, VA) with a 200 Å gold-palladium layer (80:20) and examined in a Hitachi Model S520 scanning electron microscope.

For studies at different osmolalities, cells were first equilibrated for 15 min in the same sucrose suspensions as used in the ROT studies. Cells were then fixed by the same procedure as described above but using modified versions of the cacodylate buffer (60 mM, pH 7.3 with no NaCl), adjusted to the appropriate osmolality with sucrose.

2.4. Transmission electron microscopy

Ultra-thin sections of untreated and HMBA-treated cells were prepared by centrifuging $\approx 10^7$ cells of each sample at 1200 *g* min, fixing the pellets overnight at 4°C in Millonig's phosphate buffer containing $CaCl_2$ and 3% glutaraldehyde, and washing the resulting fixed pellets at room temperature (22°C) in Millonig's buffer for 1 h. The pellets were next fixed in 2% OsO_4 for 2 h, washed in Millonig's buffer for 1 h, dehydrated in a stepwise series (50%, 70%, 95% and 100) of ethanol and soaked with propylene oxide for 30 min. They were then placed into a 1:1 mixture of propylene oxide: Mollenhauer's Epon-Araldite for 2 h, into a 1:3 mixture of the same agents for 12 h, and then finally embedded in pure Epon-Araldite resin. Embedded pellets were heat-cured at 60°C and 80°C for 1 day each.

Ultra-thin sections (900–1100 Å) were cut with a DuPont diamond knife or a Sorvall MT-2-B ultramicrotome. Sections were post-stained with saturated uranyl acetate in 50% ethanol for 10 min, then in Reynold's lead citrate for 10 min. The stained sections were then supported on copper grids without membranes and examined in a Phillips 410-G transmission electron microscope at 60 kV using original magnifications of 800 × –15 000 ×.

For studies at different osmolalities, cells were first equilibrated for 15 min in the same sucrose suspensions as used in the ROT studies and then fixed using glutaraldehyde and OsO_4 solutions with appropriately adjusted osmolalities. The pellets were dehydrated, embedded, sectioned and stained using the procedures described above.

2.5. Data analysis and modelling

Expressions for the ROT torque, ROT rate and the cell complex permittivity based on the single shell dielectric model are given in Appendix A. Equations (A-3) and (A-4) allow theoretical ROT spectra to be calculated from given cell dielectric parameters; however, it is impractical to perform the inverse procedure for direct calculations of dielectric parameters from experimental ROT data. Therefore, an optimised parameter algorithm was used to determine the best fit of Eqs. (A-3) and (A-4) to experimental data and thereby to provide estimates for the cellular dielectric parameters. This was achieved by minimising the sum of the squared deviations (the residual sum) between experimental ROT rates, R_{exp}, and those predicted from estimated parameters, R_{est},

$$\text{Min} \sum_i \left[R_{\text{est}}(\omega_i) - R_{\text{exp}}(\omega_i) \right]^2 \tag{1}$$

where i stands for each experimental point. This procedure provided estimates for the effective membrane specific capacitance, C_{spec}, and conductance, the conductivity and permittivity of the cell interior and the electrode geometry constant k (see Appendix for definitions). C_{spec} is the membrane capacitance per unit area and is equal to ϵ_{mem}/d for a spherical shell model. This parameter was calculated instead of the membrane permittivity ϵ_{mem} and thickness d because the factor ϵ_{mem}/d determines the ROT spectra, and it is not possible to separate these terms for the small values of d found in mammalian cells. In this article, we concentrate on the membrane aspects of the cells; the cytoplasmic parameters will form the subject of a later publication.

The non-linear regression analysis defined in Eq. (1) was performed using the Nelder-Mead simplex method [30] for each ROT spectrum obtained. A regression coefficient,

$$\rho = 1 - \frac{\sum_i \left(R_{\text{est}}(\omega_i) - R_{\text{exp}}(\omega_i) \right)^2}{\sum_i R_{\text{exp}}(\omega_i)^2} \tag{2}$$

was used to examine the degree to which the derived parameters fitted experimental ROT spectra. A value of ρ close to unity implied a good fit between the theoretical model and the experimental data. Estimates were also made of the confidence limits of each parameter value derived from the least-squares analysis. Because of the non-linearity of the equations that relate cell dielectric parameters to the ROT spectra (see Appendix), this analysis was done for individual parameters by a method of approximate confidence contours for non-linear systems [31]. Upper and lower limits for each parameter value were obtained numerically based on the sensitivity of the residual sum (Eq. (1)) to changes in that parameter. These limits were computed for a confidence level of 90%.

3. Results

3.1. Rotation spectra

ROT spectra of untreated and HMBA-treated DS19 cells were measured between frequencies of 10 kHz and 100 MHz at four points per decade. Typically 15 to 20 individual cells were studied for each treated and untreated sample in each of the five osmolalities (a total of 162 complete cell spectra for the work reported here). Typical ROT rate spectra normalised against the square of the applied voltage (RMS) for untreated and HMBA-treated cells are shown in Fig. 1 for the 300 mosmol/kg condition (physiological tonicity). Cells exhibited antifield rotation at frequencies below about 5

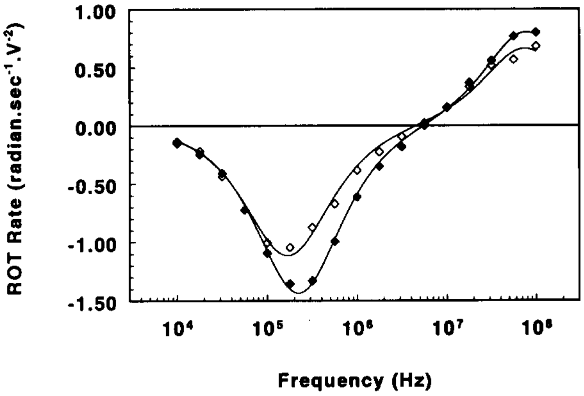

Fig. 1. ROT spectra of untreated (◇, radius $r = 5.4$ μm) and HMBA-treated (♦, $r = 5.0$ μm) DS19 MEL cells suspended in a medium of conductivity 560 μS/cm and osmolality 300 mosmol/kg. Each point represents the average of four separate stopwatch measurements. Continuous curves show best fits of the single-shell dielectric model (Eqs. (A-3) and (A-4)), determined as explained in the text. The regression coefficient, ρ (Eq. (2)), was 0.994 and 0.999 for untreated and HMBA-treated cells, respectively. Parameters, with 90% confidence limits shown in parentheses, derived from the curve fits are as follows: (a) untreated cell: $C_{\text{spec}} = 1.76$ (1.64–1.89) μF/cm^2, $G_{\text{mem}} = 7.78$ (3.85–11.6) mS/cm^2, $\epsilon_{\text{int}} = 87$ (71–104) and $\sigma_{\text{int}} = 8.9$ (7.7–10.5) mS/cm, $k = 25$ cm^{-1}, (b) HMBA-treated cell: $C_{\text{spec}} = 1.43$ (1.38–1.47) μF/cm^2, $G_{\text{mem}} = 3.16$ (1.6–4.77) mS/cm^2, $\epsilon_{\text{int}} = 98$ (90–107), $\sigma_{\text{int}} = 9.7$ (9.0–10.5) mS/cm and $k = 28.2$ cm^{-1}.

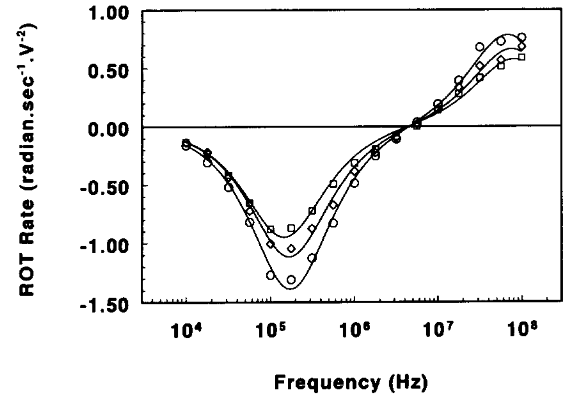

Fig. 2. Electrorotational spectra of three untreated DS19 MEL cells suspended in a medium of conductivity 560 μS/cm, and osmolalities of 210 (○, $r = 5.9$ μm), 300 (◇, $r = 5.4$ μm) and 450 mosmol/kg (□, $r = 5.4$ μm). Continuous curves were fitted as in Fig. 1 and had regression coefficients of 0.997, 0.994 and 0.995 for media of 210, 300 and 450 mosmol/kg, respectively. Best-fit parameters were as follows: (a) 210 mosmol/kg: $C_{\text{spec}} = 1.53$ (1.46–1.62) μF/cm^2, $G_{\text{mem}} = 5.56$ (2.77–8.34) S/cm^2, $\epsilon_{\text{int}} = 94$ (82–106) and $\sigma_{\text{int}} = 7.9$ (7.1–8.9) mS/cm, $k = 27.1$ cm^{-1}; (b) 450 mosmol/kg: $C_{\text{specific}} = 2.00$ (1.87–2.14) μF/cm^2, $G_{\text{mem}} = 13.8$ (6.9–20.8) mS/cm^2, $\epsilon_{\text{int}} = 84$ (69–101), σ_{int} (8.2–11.1) mS/cm and $k = 24.6$ cm^{-1}. The parameters for the 300 mosmol/kg case were the same as those in Fig. 1 legend.

Table 1
Anti-field rotation rates of DS19 cells

Sucrose concn. (mg/ml)	Osmolality (mosmol/kg)	Viscosity (kg m^{-1} s^{-1})	ROT rate	
			untreated cells (radians^{-1} V^{-2})	HMBA-treated cells radians^{-1} V^{-2})
40	140	$1.11 \cdot 10^{-3}$	1.38 ± 0.25	1.47 ± 0.21
62.5	210	$1.18 \cdot 10^{-3}$	1.24 ± 0.20	1.27 ± 0.26
85	300	$1.26 \cdot 10^{-3}$	1.12 ± 0.19	1.13 ± 0.25
100	370	$1.36 \cdot 10^{-3}$	1.06 ± 0.16	1.04 ± 0.18
125	450	$1.45 \cdot 10^{-3}$	0.97 ± 0.23	0.95 ± 0.20

Maximum anti-field rotation rate of an individual cell was determined from the theoretical modelling of its measured ROT spectrum. The results are means and standard deviations for cells measured at each osmolality. Osmolality and viscosity values for sucrose + 3 mg/ml dextrose solutions were calculated from data in Ref. [24].

MHz, and above this frequency cofield rotation occurred. For the suspending medium conductivity of 560 μS/cm, the antifield peak, corresponding to a rotation rate of about 1.1 radian s^{-1} V^{-2}, typically occurred at a frequency of 160 kHz for untreated cells and at 200 kHz for HMBA-treated cells. The exact frequency at which the peak occurred varied for individual cells and depended on the cell radius.

Fig. 2 shows representative ROT spectra for untreated DS19 cells at osmolalities of 210, 300 and 450 mosmol/kg. Two effects were observed with increasing medium osmolality: the cell spin rate decreased, and the antifield rotation peak shifted towards slightly lower frequency. The dependence of the mean antifield peak rotation rate on the medium osmolality is summarised in Table 1 for both untreated and treated samples. The mean cell spin rate fell from 1.38 to 0.97 radian s^{-1} V^{-2} for untreated samples when the medium osmolality was changed from 140 to 450 mosmol/kg.

The best-fit theoretical ROT spectra (see Appendix) are shown as continuous lines in Figs. 1 and 2, together with the regression coefficients ρ. The values obtained for ρ are larger than 0.985 for the majority of the ROT spectra, suggesting that the theoretical curves fit the experimental data quite well. This demonstrates the applicability of the theoretical model in analysing the experimental ROT spectra. Analysis of the individual parameter statistics showed that the true value of the membrane capacitance was typically within 8% of the value derived from the best-fit with a 90% confidence level (see legends to Figs. 1 and 2).

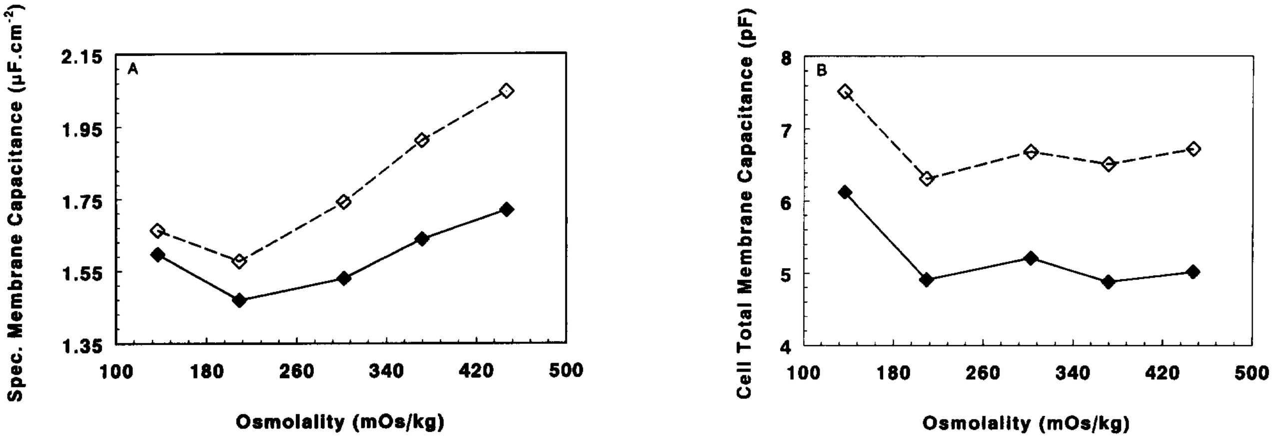

Fig. 3. Dependence of (A) mean specific and (B) mean total capacitances for untreated (◇) and HMBA-treated (◆) cells on the suspension osmolality.

Table 2
Specific and total membrane capacitances for DS19 cells and geometry factors

Osmolality (mosmol/kg)	Untreated cells				HMBA-treated cells			
	N	C_{spec} (μF/cm^2)	C_{tot} (pF)	k (cm^{-1})	N	C_{spec} (μF/cm^2)	C_{tot} (pF)	k (cm^{-1})
140	15	1.67 ± 0.19	7.52 ± 1.61	26.10 ± 2.00	26	1.60 ± 0.14	6.13 ± 1.34	27.58 ± 0.83
210	15	1.58 ± 0.12	6.32 ± 1.31	25.45 ± 1.38	15	1.47 ± 0.11	4.91 ± 1.28	26.57 ± 1.58
300	13	1.74 ± 0.20	6.69 ± 1.50	24.95 ± 2.03	18	1.53 ± 0.15	5.21 ± 1.21	25.32 ± 2.36
370	11	1.91 ± 0.24	6.52 ± 1.59	25.17 ± 2.18	20	1.64 ± 0.20	4.88 ± 1.27	24.95 ± 2.08
450	16	2.05 ± 0.17	6.83 ± 1.45	24.44 ± 2.37	13	1.72 ± 0.21	5.02 ± 1.30	24.69 ± 2.46

Specific membrane capacitance C_{spec} and geometry factor k were determined for individual cells from the theoretical modelling of its measured ROT spectrum. The individual cell total capacitance is calculated using Eq. (3) from C_{spec} and measured cell radius r. The results are means and standard deviations for cells (N is the number of measured cells) under each measurement condition.

3.2. Membrane capacitance

Table 2 summarises the theoretical curve-fitting results for the geometry factor k of Eq. (A-3) and the membrane specific capacitance for both untreated and HMBA-treated DS19 cells at the five osmolalities studied. The dependence of the mean capacitance on the osmolality, plotted in Fig. 3A, has several trends:

(1) Cell membrane specific capacitance values were significantly higher than the value of 1 μF/cm^2 often cited for biological cells [32], especially at the higher osmolalities investigated. For example, the mean value for untreated DS19 cells at 450 mosmol/kg was 2 μF/cm^2.

(2) For all the osmolalities studied, the mean capacitance value for DS19 cells was lower following HMBA treatment. The capacitance difference between untreated and treated samples increased from about 7% at 210 mosmol/kg to about 19% at 450 mosmol/kg. Statistical analysis (t-test for the difference of two means [33], 28 or more degrees of freedom) indicated that these differences were significant at $p < 0.005$, $p < 0.005$ and $p < 0.0001$ levels for osmolalities of 300, 370 and 450 mosmol/kg, respectively (p is the probability that the two means are identical). While the mean capacitance of treated cells was also lower than for treated cells at 210 and 140 mosmol/kg, the difference was statistically less significant ($p < 0.02$ and $p < 0.2$, respectively) for these cases.

(3) The specific capacitance values for cells increased with increases in osmolality except at the lowest osmolality studied (140 mosmol/kg). When the osmolality was changed from 210 to 450 mosmol/kg, the capacitance of untreated cells increased by about 30%, whilst that of HMBA-treated cells showed an increment of only 17%.

(4) It is evident from the standard deviations in Table 2 that relatively large variations existed in the membrane capacitance under each measurement condition. In many cases, this variation exceeded 30% within a sample group. Since the true capacitance value for each cell was within 8% of its derived values at the 90% confidence level, such large variations within each sample group reflected true differences in individual cell properties.

The total membrane capacitance, C_{tot}, is defined as the product of the cell surface area ($4\pi r^2$ for a cell of radius r) and the specific capacitance as

$$C_{tot} = 4\pi r^2 C_{spec} \tag{3}$$

It is evident from Table 2 and Fig. 3B that for both untreated and HMBA-treated cells, the mean total capacitance (6.6 pF and 5.0 pF for untreated and HMBA-treated cells, respectively) was essentially independent of the suspending medium's osmolality except at the lowest osmolality, where it increased by about 14% and 22% for untreated and HMBA-treated samples, respectively. The total capacitance of DS19 cells decreased by about 32% following HMBA treatment.

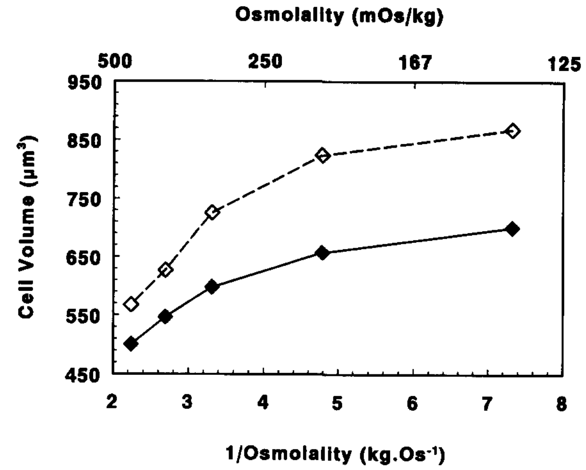

Fig. 4. Mean volume (average of at least 130 cells at each osmolality) of untreated (◇) and HMBA-treated (◆) DS19 cells as a function of the reciprocal of the medium osmolality. A linear plot would indicate that cells behaved as ideal osmometers according to the Boyle-Van 't Hoff relationship.

3.3. Cell volume dependence on suspending medium osmolality

Cell sizing was accomplished under identical conditions to those used for ROT measurements using the same image analysis methods. Mean volumes for at least 130 cells at each osmolality are shown in Fig. 4. It is clear that an inverse relationship existed between cell volume and suspension osmolality for both untreated and HMBA-treated cells. However, while untreated cells decreased in volume by about 22% when they were shifted from 300 to 450 mosmol/kg medium (to about 1.5 × physiological tonicity), HMBA-treated cells decreased in volume by only 16%. For a shift from 300 to 140 mosmol/kg (to about 0.5 × physiological tonicity), cells increased in volume by 20% and 17% for the untreated and HMBA-treated cases, respectively. Neither sample behaved as predicted by the Boyle-Van 't Hoff relationship (see Discussion) [19,34].

3.4. Surface morphology of MEL cells

To study the possible relationship between membrane capacitance and cell surface structure, we used SEM to analyse MEL cells as a function of both HMBA treatment and osmotic manipulation. Fig. 5A shows untreated and Fig. 5B HMBA-treated DS19 cells prepared from isotonic (300 mosmol/kg) medium. In each case, cells were heterogeneous in size and

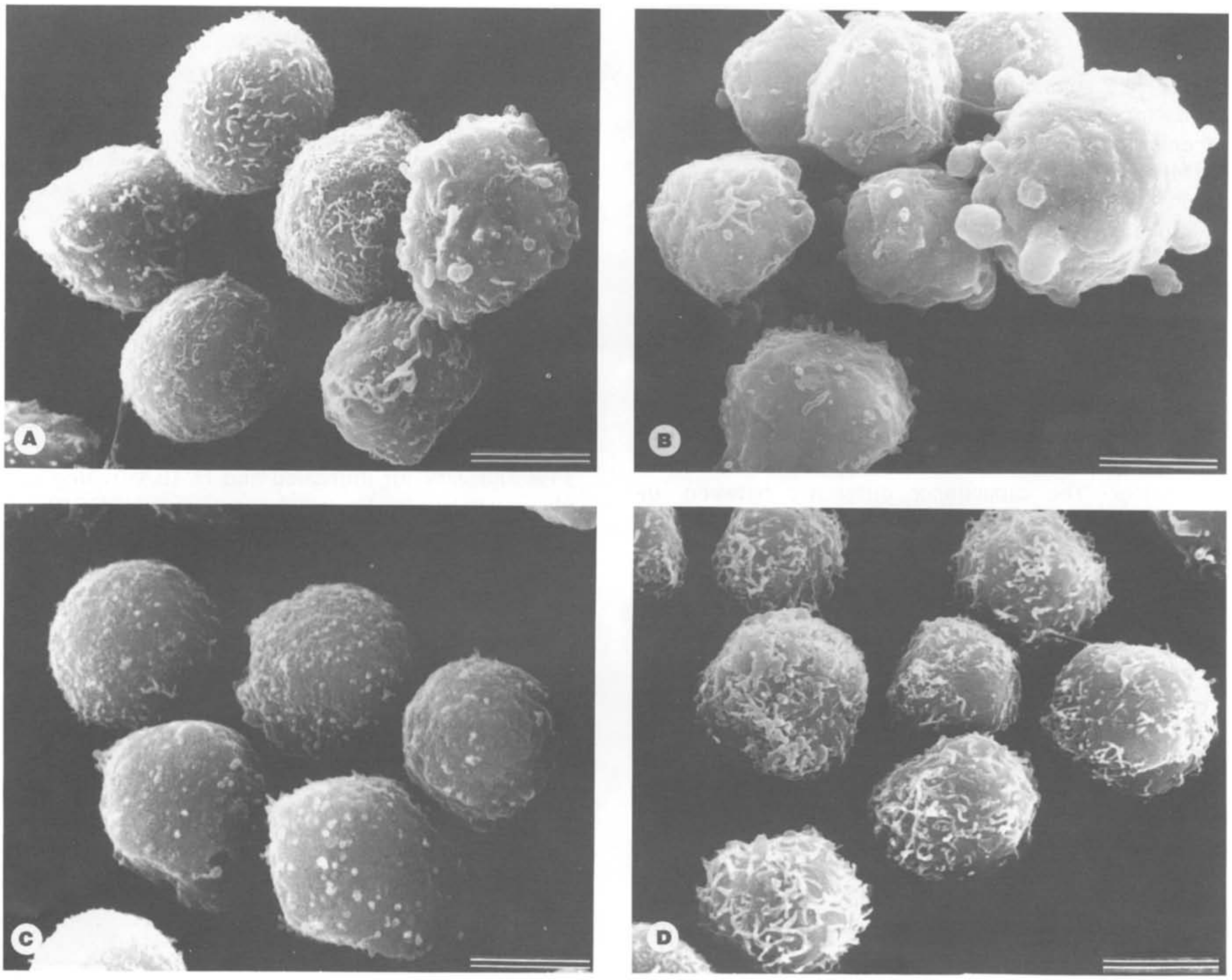

Fig. 5. Scanning electron micrographs of cells as a function of HMBA treatment and osmolality. Bar length = 5 μm. (A) Untreated DS19 cells fixed in isotonic media (300 mosmol/kg). Although most cells exhibit complex, frequent and relatively delicate microvilli, a few demonstrate a combination of coarse microvilli, blebs and smoother surfaces. Such heterogeneity is typical of untreated DS19 cultures. (B) DS19 cells after 3 days of HMBA treatment fixed under the same isotonic conditions as in (A). Most cells have few microvilli and these are generally coarser in texture than in untreated cells. Small and large blebs are evident with much of the surface area smooth and in some aspects planar in nature. (C) Untreated DS19 cells fixed at 210 mosmol/kg. Relatively granular surfaces, free of extended microvilli are evident with microvilli segments barely protruding above the cell surfaces. (D) Untreated DS19 cells fixed at 450 mosmol/kg demonstrate relatively extensive, somewhat elongated, and intertwined villi which appear to be 'matted' in some areas.

morphology. Approx. 85% of cells in the untreated sample exhibited a dense surface display of small microvillus projections with rare scattered blebs. By comparison, approx. 70% of the cells in HMBA-treated samples exhibited generally smooth, non-villus, somewhat planar surfaces with increased numbers of blebs, typically of the order of 0.5–1 μm size. This alteration in surface features over the three days of HMBA treatment involved the progressive loss of villus structure accompanied by an increase in the number and size of blebs. Approx. 15% of the untreated cells and 30% of the HMBA-treated cells exhibited surface morphological characteristics of their counterparts.

Surface morphology of the cells strongly depended upon the osmolality of the suspending medium. Figs. 5A, C and D show untreated cells fixed at 300, 210 and 450 mosmol/kg, respectively. Cells suspended at 450 mosmol/kg demonstrated uniformly abundant microvilli that appeared to be longer and, in some areas, more interdigitated or matted than those at 300 mosmol/kg. The cells fixed at 210 mosmol/kg exhibited a somewhat granular surface relatively free of microvilli, with short segments of microvilli potruding above the cell surface in scattered areas.

Transmission electron micrographs were used to establish whether the interiors of microvilli and blebs were contiguous with the cytoplasm or were separated from it by membranes. The aim was to determine whether these surface components should behave electrically as parts of a single, continuous cytoplasmic membrane or as small, isolated subcompartments. Fig. 6A shows an untreated DS19 cell and reveals that the microvilli had interiors freely connected to the cytoplasm. Fig. 6B, derived from a treated cell, demonstrates that the blebs were also in continuity with the cytoplasm and indeed in several areas can be seen to contain cytoplasmic organelles and endoplasmic reticulum. Thus, plasma membrane formed a single, continuous surface over each cell and should have been detected as such through dielectric observations.

4. Discussion

4.1. ROT rate

It follows from the theoretical analysis in Appendix A (Eq. (A-3)) that the cell ROT rate depends on the cell's dielectric properties, the suspending medium's viscosity and the electric field distribution. The dependence on viscosity can be observed in the experimental data shown in Table 1. As the medium osmolality was increased from 140 to 450 mosmol/kg by the addition of sucrose, the dynamic viscosity increased from $1.1 \cdot 10^{-3}$ to $1.45 \cdot 10^{-3}$ $\mathrm{kg\,s^{-1}\,m^{-1}}$), and the grand mean peak rotation rate decreased from 1.44 to

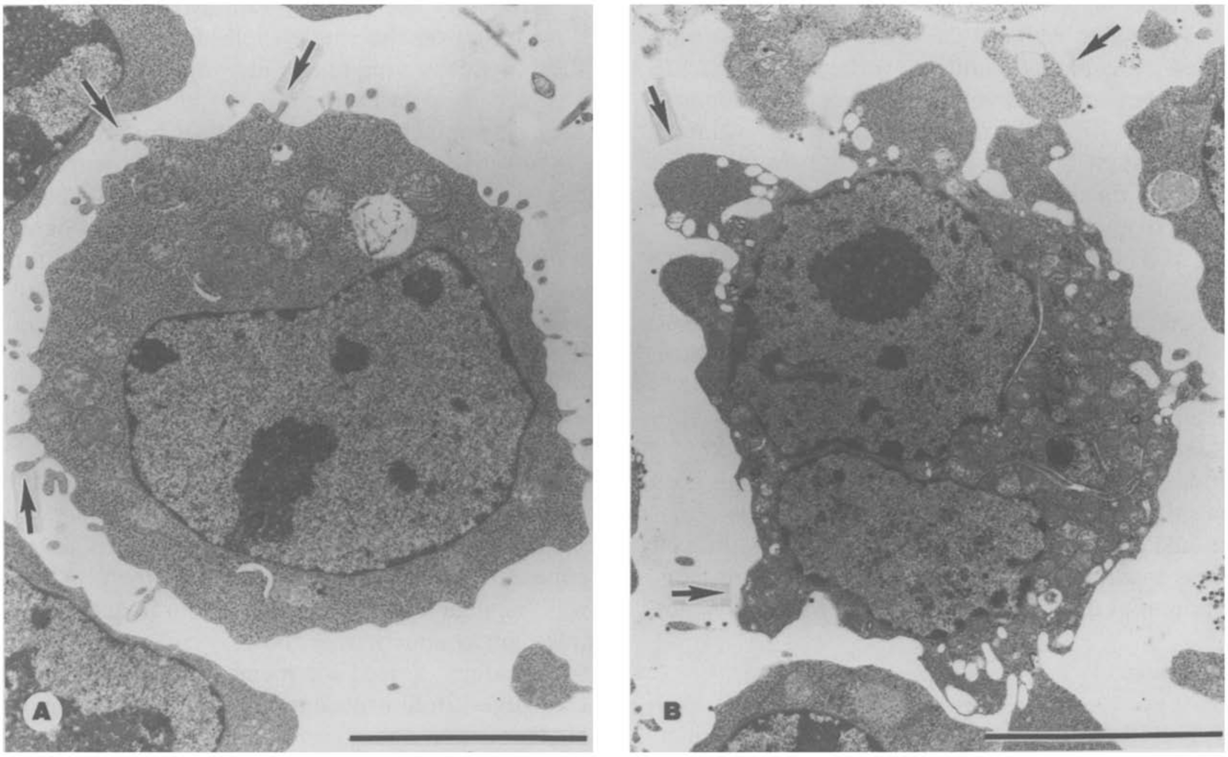

Fig. 6. Transmission electron micrographs of untreated and 3 day HMBA-treated DS19 cells. Bar length = 5 μm. (A) Untreated cell showing that the microvilli exhibit granular, ribosome-containing interiors (arrows) that are in continuity with the cytoplasm. (B) HMBA-treated cell showing that the blebs (arrows) are also in continuity with the cytoplasmic space and share vesicles, ribosomes and tubular reticulum.

0.96 radian $s^{-1} V^{-2}$. This decrement in cell spin rates was approx. 12% larger than predicted by Eq. (A-3), which takes into account the dynamic viscosity and cell dielectric changes but ignores any frictional interaction between the cells and the glass substrate. This interaction affects the accuracy, though not the validity, of Eq. (A-3). Friction may have been different for cells with distinct surface morphologies (see Fig. 5 for the comparison of untreated and HMBA-treated cells) and for the different buoyancy factors corresponding to the various osmolalities of sucrose employed. These factors could have accounted for the observed 12% deviation from Eq. (A-3).

4.2. *ROT field strength*

The mean values of the geometry factor k, determined by the electric field distribution [35] and cell position in the polynomial electrode system, were obtained from theoretical analyses of ROT spectra and are summarised in Table 2. Small variations in k under each experimental condition indicated that the electric field under the quadrature signal excitation was sufficiently uniform in the central region between the four electrodes. The apparent decrement in k in the high osmolality case probably resulted from the above-mentioned frictional effect. Based on the mean value of k for all the cells studied, the rotating electric field strength was calculated to be about 25 V/cm for a 1 V RMS voltage signal applied to each of the four electrodes. This value is about 2.8-times smaller than that calculated by assuming a uniform voltage drop of 2.828 V (2 × the peak applied voltage) between the opposite electrode tips of 400 μm separation. This value is reasonable when fringing effects caused by the small thickness of the electrodes (0.1 μm) relative to the large cell diameter (12 μm) are taken into account. Indeed, M. Hughes of our laboratory has made preliminary calculations on the electrode system employed here using the surface charge density method and shown that the field strength at a plane 6 μm above the electrode surface is 33 V/cm for a 1 V RMS quadrature signal excitation, in good agreement with our estimate of 25 V/cm. This field corresponded to a maximum induced AC voltage of 15 mV across the cell plasma membrane, and it is reasonable to assume that such a small field would not physically stress the cell since it is smaller by a factor of 3 than the transmembrane potential difference reported for MEL cells [36].

4.3. *Shell model*

The fact that the regression coefficients obtained from the simulation are close to 1 (see Figs. 1 and 2 legends) indicates that the dielectric properties of individual cells could be described by a single dielectric relaxation, as embodied in the single shell model. However, for some of the cells investigated, the experimental ROT antifield peaks were not symmetrical, and relatively large deviations between theoretical fits and experimental data occurred in the frequency range between 400 kHz and 10 MHz. These deviations reflected the fact that cellular structure is far more complicated than was taken into account by the spherical shell model, which ignores membrane inhomogeneity and cytoplasmic and nuclear structural features.

To make meaningful deductions from the ROT data, it was important to ensure that the dielectric parameters derived from the non-linear analysis represented unique solutions. As a test, theoretical ROT spectra were generated for 100 sets of dielectric parameters ranging within a factor of 3 of the values expected physiologically. These synthetic spectra covered the same frequency range and had the same number of points per decade as were measured in the cell experiments. Gaussian random errors were then added, and the spectra were fitted using the non-linear regression procedure. The parameters derived from the curve fit were then compared to the input values and good agreement was found (Gascoyne, P.R.C. and Wang, X.-B., to be published). For example, relative errors added to the data having a normal distribution, a variance of 0.05 and a mean of zero resulted in derived membrane capacitance values within 6% of their true values at a 90% confidence level.

To further examine the validity of the fitting procedure based on the single shell model (see Appendix), the crossover frequency at which the DEP force changed its polarity (below 300 kHz) was experimentally determined to a 5% accuracy for each cell. This crossover frequency was then compared with that predicted from the derived parameters by calculating the real part of induced dipole moment (see Appendix). It was found that the predicted and experimentally-determined crossover frequencies agreed within 10% for 95% of cases. When agreement was not obtained, the data were rejected.

4.4. *Membrane electrical properties and biological significance*

As was expected, the membrane conductivity was several orders of magnitude less than the medium conductivity, and its contribution to the ROT spectra was negligible under our measurement conditions (medium conductivity = 560 μS/cm). As a result, the small values derived for membrane conductance from the curve-fitting procedure were unreliable (as judged by the upper and lower limits at a 90% confidence level) and will not be discussed here.

As indicated in Table 2, the membrane capacitance obtained from analysis of our ROT spectra for different cells showed considerable variation within each sample. Several factors could have contributed to this variability. Firstly, DS19 is a transformed cell line that exhibits the typical heterogeneous cell morphology and ploidy [37] seen in many cancers. Secondly, cells were obtained from asynchronous log phase cultures and so the population was mixed with respect to cell cycle phase. Thirdly, about 10% of cells in untreated samples underwent spontaneous differentiation, while only 60% of cells synthesised haemoglobin in response to HMBA treatment after 72 h [38]. It follows that the DS19 samples were heterogeneous and exhibited differences in cell size and membrane conformation and composition and this is considered to be the source of the observed variation of membrane capacitance within sample groups.

As pointed out earlier, the specific capacitance values obtained here are in general larger than the frequently-quoted value for mammalian cell plasma membranes of $\approx 1\ \mu\mathrm{F/cm}^2$ [32]. It is therefore of interest to analyse the factors contributing to such large values. According to the fluid-mosaic model, the membrane consists of a lipid bilayer into which proteins and other biomolecules are incorporated [16]. Electrically, the capacitance and conductance of the lipid bilayer function in parallel with those of the protein and other portions of membrane. Thus, the specific capacitance of the membrane, C_s, can be written as

$$C_\mathrm{s} = \alpha C_\mathrm{sl} + (1-\alpha) C_\mathrm{sn} \tag{4}$$

where C_{sl} and C_{sn} are the specific capacitance of lipid and 'other' components, respectively, and α is the proportion of lipid in the membrane measured by area. 'Other' components comprise the membrane proteins, cholesterol and other elements that span all or part of the barrier between cytoplasm and the cellular space. We shall briefly consider these various contributions.

Dielectric measurements indicate that for artificial lipid bilayers [39–41], the differences in their capacitance is mainly determined by the nonpolar hydrocarbon groups, with little dependence on the polar headgroups. Furthermore, the lipid bilayer capacitance has been shown to be inversely proportional to the number of carbon atoms in the lipid hydrocarbon chain. Based on the hydrocarbon chain length estimated from molecular models and from X-ray and other measurements, a value of 2.0 to 2.2 can be calculated for the relative permittivity of the hydrocarbon core, and this value has now become commonly accepted [42]. Assuming that their hydrocarbon groups have the same structural arrangement and thickness as artificial membranes, the lipid bilayer components of mammalian cell membranes can then be calculated to have a specific capacitance of about $0.73\ \mu\mathrm{F/cm}^2$ for an 18-carbon chain and $0.82\ \mu\mathrm{F/cm}^2$ for a 16-carbon chain. For the reported lipid compositions of mammalian cells in general and for DS19 in particular [43–44], 16- and 18-carbon-chain backbones dominate the bilayer composition and a value of $0.78\ \mu\mathrm{F/cm}^2$ may be taken as a reasonable estimate for the lipid specific capacitance. Cholesterol, which resides close to the aqueous interface of the lipid bilayer, has been shown experimentally to have little effect on capacitance [40].

The contribution of integral proteins to the dielectric properties of the plasma membrane is dominated by the non-polar amino acid residues in the hydrophobic transmembrane region. Based upon calculations of the polarisability of these non-polar amino acids [45] and of measurements on hydrophobic amino acid homopolymers [46], a relative permittivity of up to 2.8 may be assigned to this region. If it is assumed that the thickness of the hydrophobic regions of the lipid bilayer and non-polar integral protein regions are the same, the specific capacitance of the protein regions is calculated to be up to $1.04\ \mu\mathrm{F/cm}^2$. Some proteins contain aqueous pores; however, the small dimensions of these pores result in an increase in protein capacitance of only 5% even if all proteins in the membrane contain them [42]. Peripheral proteins and regions of the integral proteins that lie outside the hydrophobic core contribute little to the membrane capacitance.

Placing these values into Eq. (4), and assuming that 40% [43] of the plasma membrane area is accounted for by protein ($\alpha = 0.6$), then a value of $0.94\ \mu\mathrm{F/cm}^2$ is derived for the specific plasma membrane capacitance C_s. Since the dielectric parameters derived for the cell membrane are averaged over the whole cell, it is unimportant whether the membrane is laterally homogeneous or contains localized lipid or protein domains.

In deriving the above values for the membrane specific capacitance, we have assumed that the plasma membrane is smooth. In this case, the specific capacitance would be ϵ_mem/d, and the total capacitance of a smooth, spherical cell would be $C_\mathrm{tot} = 4\pi r^2 \epsilon_\mathrm{mem}/d$ (where the membrane thickness is d and its permittivity ϵ_mem). In reality, a cell has surface features such as microvilli, folds, ruffles, and blebs (see Figs. 5 and 6), and the total area of membrane covering its surface will be larger than $4\pi r_\mathrm{meas}^2$ by a factor ϕ_mem, where r_meas is the apparent radius of the cell determined by light microscopy and ϕ_mem is the membrane-folding factor, which exceeds unity for a rough surface. The total membrane capacitance for a real cell is therefore $C_\mathrm{tot} = \phi_\mathrm{mem} 4\pi r_\mathrm{meas}^2 \epsilon_\mathrm{mem}/d$. The shell model employed to analyse the data did not take this folding into account and the specific capacitance derived from the ROT data for each cell would therefore exceed that of a smooth membrane by the factor ϕ_mem. This concept was invoked by Arnold and his co-workers to account for the changes observed by electrorotation in the membrane capacitance of T-and B-lymphocytes following mitotic stimulation and of cultured cells under osmotic stress [19,20].

Based on these membrane-folding considerations, SEM photographs were taken to quantitate ϕ_{mem} for our cell populations. Estimates of the total surface area were made from SEM photographs of a number of cells, taking into account the microvilli and other structures observed on their surfaces (see Figs. 5). Based on such structures, it was found that the true surface area in the isotonic (300 mosmol/kg) medium for most (85%) cells in untreated DS19 samples ranged from 1.5 to 2.0 times that for smooth, spherical particles of similar radius ($\phi_{\mathrm{mem}} = 1.5$ to 2.0). In the case of hypertonic solutions, which enhanced the microvilli, ϕ_{mem} was as high as 2.4. Furthermore, smaller-scale membrane features were not taken into account, so that even these values for ϕ_{mem} are underestimates. This implies that the specific capacitance can be expected to be at least as large as 2.25 $\mu F/cm^2$ in DS19 cells if their membrane has a capacitance of 0.94 $\mu F/cm^2$ when it is smooth. We conclude, therefore, that the complexity of the membrane surface mainly accounts for the large capacitance values observed in this study. In support of this conclusion, we performed ROT measurements on peripheral, normal murine erythrocytes (from 14 month-old, male C57BL/6-A^{vy} mice) at 300 mosmol/kg under identical conditions to our DS19 observations. For each cell, ROT was measured about an axis perpendicular to the convex faces of the erythroid disc so that it closely mimicked the rotation of a sphere as assumed in the dielectric shell model. We obtained a specific capacitance of 0.83 ± 0.08 $\mu F/cm^2$ (at a 90% confidence level) reflecting the smooth surfaces and homogeneous morphology of these cells, and supporting the predicted capacitance value for this case. This value for the specific capacitance of erythrocytes agrees with that determine by the micropipet and suspension techniques [47,48].

At physiological tonicities, the mean specific capacitance of DS19 cells decreased from 1.74 to 1.53 $\mu F/cm^2$ following HMBA treatment. As described in the SEM results section, a marked reduction in microvilli but an increase in larger blebs (Fig. 5B) occurred for the surfaces of about 70% of the cells in HMBA-treated samples. The membrane folding factor ϕ_{mem} of these cells estimated from the SEM pictures ranged from 1.2 to 1.5. Thus, the mean membrane-specific capacitance fell by approx. 14% and the folding factor by about 29% following HMBA treatment. These reductions are consistent with one another when the heterogeneity in the surface morphology of the samples is taken into account. The biological significance of the microvillous features in untreated DS19 cells, the blebbing in treated cells, and the changes in surface area following treatment are not clear. However, microvilli increase cell surface area and represent a potential reservoir of membrane that may facilitate cell division and rapid changes in cell morphology [21]. Transformed and mitotic cells and those treated with tumour promoters usually exhibit abundant microvillous features [49].

MEL cells have been proven to be extremely useful models for studying the process of erythroid differentiation [50]. They are derived by transformation by the Friend erythroleukaemia virus [51] and are considered to be arrested in differentiation approximately at the stage of colony-forming unit (CFU-E) cells [52] but can be induced to resume their program of erythroid differentiation by a variety of agents including HMBA and DMSO [53]. After 72 h of HMBA treatment in suspension culture in the absence of fibronectin, roughly 60% of DS19 cells show evidence of haemoglobin expression [38], indicative of the erythroblast phenotype, yet cells still exhibited log-phase growth and culture densities that were almost identical to their untreated counterparts (growth curve and flow cytometric cell cycle analysis data not shown). These similarities in growth characteristics allowed direct comparison between treated and untreated cell samples.

A striking feature of normal erythroid differentiation is the marked shift that occurs in membrane morphology from the undifferentiated surface characteristics of CFU-E stage cells (which exhibit numerous microvilli and filopodia that protrude from the cell body) to the mature erythroid characteristics (smooth, discoid surface). These changes in membrane features accompany, and have been attributed to, the development of a sub-membrane skeleton composed predominantly of spectrin (which constitutes 30% of the membrane protein of mature erythrocytes), and actin, ankyrin, band 3 and other proteins. After the first 72 h of differentiation treatment, MEL cells accumulate equal amounts of α- and β-spectrin and band 3 protein accumulation begins [21]. The SEM and TEM photographs (see Figs. 5 and 6) show changes in DS19 at this stage of treatment that are compatible with these early stages of the development of the membrane skeleton, namely the loss of microvilli and a marked smoothing of the membrane surface texture.

Other evidence supports the proposition that these membrane surface alterations result from the development of a membrane skeleton. The conductivity of the membrane observed by dielectrophoresis measurements falls at least 5-fold following induced differentiation [13]. Experiments on inside-out vesicles derived from erythrocytes show that the leakage of the membrane is inversely proportional to the integrity of the spectrin membrane skeleton and so, the observed drop in membrane conductivity following the induced differentiation of DS19 cells suggested the development of such a structure. Furthermore, membrane fluidity determined by electron spin resonance falls more during HMBA treatment of DS19 than can be accounted for by measured changes in membrane lipid composition alone [44,54,55] but to an extent compatible with an increased structural protein content of the membrane.

4.5. Variation of membrane capacitance with osmolality

In order to study the structural properties of the membrane further, we investigated the responses of untreated and HMBA-treated DS19 cells to osmotic changes. It is helpful to consider the osmotic properties of a simple, ideal (Van 't Hoff) particle, which has a single, flexible membrane that is permeant to water but not to ions. When suspended in a physiologically-isotonic medium, such an ideal particle will be a perfect sphere. When the particle is suspended in a hyper-osmotic medium, water molecules will leak out and its volume will decrease until its internal osmolality matches that of the external medium. Since the osmolality is approximately proportional to the ionic concentration, a doubling of the external osmolality will cause the particle volume to be reduced by half (the ideal Boyle-Van 't Hoff relationship [34]) and its radius will be reduced by about 20%.

If the membrane area and thickness is conserved, then the total capacitance will be the same as it was initially but the membrane will become wrinkled and its specific capacitance (capacitance per unit area) will increase by a factor of about 1.6. Theoretical ROT spectra for these two osmotic conditions are shown in Fig. 7. The antifield ROT peak can be seen to be shifted to a lower frequency as the suspension osmolality is increased.

We found that this effect occurred, qualitatively, in the osmolality studies on DS19 cells over the range of 210 to 450 mosmol/kg for both untreated and HMBA-treated cells (see Fig. 3B for the mean total capacitance and Fig. 4 for cell volume). However, the variations in the specific membrane capacitance and volume with changing osmolality were significantly smaller than expected for the ideal case considered above. For example, an increase in osmolality from 300 to 450 mosmol/kg should, ideally, result in a volume decrement of about 34% and a specific capacitance increment of about 30%. In reality, volume decrements of only 22% and 16% and specific capacitance increments of only 18% and 12% were observed experimentally for untreated and HMBA-treated cells, respectively.

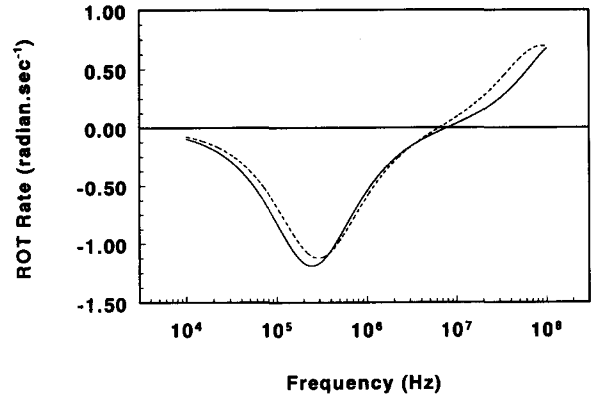

Fig. 7. Theoretically-calculated ROT spectra illustrating the effects of membrane folding when a particle having a semi-permeable, non-elastic membrane experiences a doubling of its external osmolality. The particle is assumed to exhibit an ideal Boyle-Van 't Hoff response and no adjustments are applied to the data to account for possible changes in hydrodynamic resistance due to morphological changes in the cell surfaces. Spectra were calculated from Eqs. (A-3) and (A-4) using the following parameters: (1) initial osmolality case (- - - - - -): $r = 6$ μm, $C_{\mathrm{spec}} = 0.9$ μF/cm^2, $\sigma_{\mathrm{int}} = 10$ mS/cm; (2) doubled osmolality case (———): $r = 4.76$ μm, $C_{\mathrm{spec}} = 1.43$ μF/cm^2, $\sigma_{\mathrm{int}} = 20$ mS/cm. In both cases, $G_{\mathrm{mem}} = 4.44$ mS/cm^2, $\epsilon_{\mathrm{int}} = 78$, $k = 25$ cm^{-1} and medium viscosity $= 1.26 \cdot 10^{-3}$ kgm^{-1}s^{-1}. Details regarding the change of particle dielectric properties upon doubling the osmolality are discussed in the text.

Two differences between DS19 cells and ideal particles may account for these deviations. Firstly, DS19 cells have internal structures that will imbue them with a bulk modulus that provides a mechanical reaction to external forces. Such mechanical responses, which tend to lessen the response of the cell to osmotic stress, are not taken into account in the ideal model. It is likely that this bulk modulus will depend on both the membrane skeleton and the cytoskeleton and that the change of article volume with external pressure will be non-linear at the extremes of both compression (because of the presence of internal organelles) and expansion (because of the limited capability of the membrane to stretch). Secondly, it has been observed that many cell types have the ability to undergo a dynamic volume alteration when they are placed in anisotonic media, pumping ions across their membranes in direct violation of the ion-impermeant assumption implicit in the Boyle-Van t' Hoff relationship. This response, which normally takes about 15 min to complete, lowers the ionic gradient between the inside and outside of the cell and thereby tends to reduce the volume response from that anticipated for an ideal particle. It is likely that DS19 cells underwent such dynamic volume regulation when they were placed in anisotonic media.

As shown in Table 2, increasing osmolality from 210 to 450 mosmol/kg changed the cell membrane specific capacitance for untreated DS19 cells by 30% while the change for HMBA-treated cells was only 17% under these conditions. This is compatible with the observation that untreated cells changed their volume more than HMBA-treated cells, and both observations suggest that the bulk modulus of the DS19 cells increased during differentiation. These findings are compatible with the expected properties of a developing membrane skeleton and/or cytoskeleton structure [23]. Previous observations on temperature-sensitive transformed rat kidney cells have demonstrated that the exposure of such cells to non-permissive temperatures is associated with a progressive loss of plasma membrane microvilli and the progressive reappearance within the cells of a normal microtubular system and F-actin cable [56].

Finally, for both untreated and HMBA-treated cells, the specific capacitance increased as the osmolality was reduced from 210 to 140 mosmol/kg. This directly contradicted the prediction of the membrane folding model of capacitance for the observed volume changes occurring at this osmotic decrement. From the SEM photograph of cells at the osmolality of 210 mosmol/kg (Fig. 5C), however, it is clear that the membrane is approaching the limit of its ability to disassociate from microvilli and provide coverage for the expanding body of the cell. It is conceivable that lateral tension in the membrane under these circumstances might lead to some thinning of the membrane, a condition that would be expected to increase the membrane specific capacitance with increasing cell volume [19], though changes of only a few percent might be expected from this mechanism. Such stretching would presumably be a precursor to cell damage. Currently, we are not aware of additional mechanisms that can account for the observed increase in membrane specific capacitance at low tonicities, however an additional mechanism for increasing the total membrane capacitance (see Table 2) would be through membrane cycling though we have not attempted to examine this possibility here.

Acknowledgments

We are grateful to Jamileh Noshari for culturing the cells used in this study, to John Tame for providing the polynomial electrodes, to Kim Dulski for SEM and to Brooks Myers for TEM. We also thank Ka Lok Chan, M Hughes and Profs. T.B. Jones and K.V.I.S. Kaler for helpful discussions. The work was supported in part by grants from the State of Texas Advanced Technology Project, the Alpha Kappa Psi Cancer Bowl Fund, the UK CVCP Overseas Research Scholarship award (Y.H.) and the EEC Research Fellowship (R.H.). SEM was made possible by NIH Core Grant P30-CA16672.

Appendix A

The electrorotational torque $\Gamma(\omega)$ experienced by a spherical particle of radius r and effective, complex permittivity ϵ_p^* in a rotating electric field E is given [57,58] as

$$\Gamma(\omega) = -4\pi\epsilon_m^* r^3 \operatorname{Im}(f(\omega))E^2 \tag{A-1}$$

where ω is the angular frequency of the applied rotating field, ϵ_m is the medium absolute permittivity, and the operator Im takes the imaginary component of the Clausius-Mossotti factor

$$f(\omega) = \frac{\epsilon_p^* - \epsilon_m^*}{\epsilon_p^* + 2\epsilon_m^*}$$

This factor determines the magnitude and phase of the induced dipole moment. When $\operatorname{Im}(f(\omega)) > 0$, the induced dipole moment lags behind the applied field by more than a half period and an anti-field rotational torque is exerted on the particle. Conversely, when $\operatorname{Im}(f(\omega)) < 0$, the dipole moment lags by less than a half period, resulting in a cofield torque. (The real components of the Clausius-Mossotti factor determines the dielectrophoretic forces experienced by the particle subjected to a non-uniform electric field). The steady-state particle rotation rate $R(\omega)$ occurs when the ROT torque is balanced by the opposing viscous drag of the suspending medium and is readily derived [8] as

$$R(\omega) = -\frac{\epsilon_m E^2}{2\eta}\operatorname{Im}(f(\omega)) \tag{A-2}$$

where η is the medium dynamic viscosity. The rotating electric field is normally generated by energising more than three electrodes with phase-shifted voltage signals. Thus, the ROT rate can be further expressed in terms of the applied voltage signal V(RMS) as

$$R(\omega) = -\frac{\epsilon_m k^2 V^2}{2\eta}\operatorname{Im}(f(\omega)) \tag{A-3}$$

where k $(=E/V(\mathrm{RMS}))$ is a constant relating to the electrode geometry and the particle position inside the electrode chamber. It follows that the ROT rate is a function of the applied voltage, V(RMS), the medium viscosity, η, the electrode geometry and the particle position. More importantly, from the standpoint of cell characterisation, it depends on the difference between the dielectric properties of particle (ϵ_p^*) and its suspending medium (ϵ_m^*). Cell ROT studies involve measurement of the frequency spectrum of the cell rotation rate from which cellular dielectric parameters can then be calculated using Eq. (A-3).

Below the characteristic frequency for interfacial polarisation of the inside surface of the plasma membrane of a cell (typically ≈ 1 MHz), the applied electric field is mainly dropped across the plasma membrane. The cell then behaves as a poorly conducting sphere with a high effective permittivity, ϵ_{eff}. Under these conditions, the cell has a characteristic dielectric response time (defined as $\epsilon_{\mathrm{eff}}/\sigma_{\mathrm{eff}}$) that is larger than that of the surrounding medium ($\epsilon_{\mathrm{med}}/\sigma_{\mathrm{med}}$). As a result, the induced dipole lags behind the applied field by more than a half period (phase difference > 180°) [8,28], and antifield rotation occurs. Above about

10 MHz, the applied field penetrates the cell, which then behaves as a conducting sphere having the permittivity of the cell interior. The resulting effective dielectric response time of the cell is then smaller than that of the suspending medium, the induced dipole lags behind the field by less than a half period (phase difference < 180°), and cofield rotation occurs. Cells are heterogeneous and complicated in structure and composition and their rotational spectra reflect the dielectric characteristics of these complex features [8,59,60].

Various models have been proposed for analysing cellular dielectric properties, among which shell models have been applied most extensively [5,10,28,57,60–62]. In this work, a single shell model was used consisting of a conductive interior sphere of radius r, having a complex permittivity $\epsilon_{int}^* = \epsilon_{int} - j\sigma_{int}/\omega$, surrounded by a poorly-conducting membrane of thickness d, having a complex permittivity $\epsilon_{mem}^* = \epsilon_{mem} - j\sigma_{mem}/\omega$. In this case, the cell complex permittivity is given by

$$\epsilon_p^* = \epsilon_{mem}^* \frac{\left(\frac{r+d}{r}\right)^3 + 2\left(\frac{\epsilon_{int}^* - \epsilon_{mem}^*}{\epsilon_{int}^* + 2\epsilon_{mem}^*}\right)}{\left(\frac{r+d}{r}\right)^3 - \left(\frac{\epsilon_{int}^* - \epsilon_{mem}^*}{\epsilon_{int}^* + 2\epsilon_{mem}^*}\right)} \qquad \text{(A-4)}$$

Membrane specific capacitance and conductance are defined as ϵ_{mem}/d and σ_{mem}/d, respectively.

References

[1] Pethig, R. (1991) in Automation in Biotechnology (Karube, I., ed.), pp. 159–185, Elsevier, Amsterdam.

[2] Pohl, H.A. (1978) Dielectrophoresis, Cambridge University Press, New York.

[3] Burt, J.P.H., Pethig, R., Gascoyne, P.R.C. and Becker, F.F. (1990) Biochim. Biophys. Acta 1034, 93–101.

[4] Pethig, R., Huang, Y., Wang X.-B. and Burt, J.P.H. (1992) J. Phys. D Appl. Phys. 25, 881–888.

[5] Kaler, K.V.I.S. and Jones, T.B. (1990) Biophys. J. 57, 173–182.

[6] Washizu, M. (1990) J. Electrostat. 25, 109–123.

[7] Arnold, W.M. and Zimmermann, U. (1982) Z. Naturforsch. 37c, 908–915.

[8] Arnold, W.M. and Zimmermann, U. (1988) J. Electrostat. 21, 151–191.

[9] Fuhr, G., Rosch, P., Muller, T., Dressler, V. and Goring, H. (1990) Plant Cell Physiol. 31, 975–985.

[10] Hölzel, R. and Lamprecht, I. (1992) Biochim. Biophys. Acta 1104, 195–200.

[11] Gimsa, J., Glaser, R. and Fuhr, G. (1991) in Physical Characterisation of Biological Cells (Schutt, W., Klinkmann, H., Lamprecht, I. and Wilson, T., eds.), pp. 295–323, Verlag Gesundheit, Berlin.

[12] Wang, X.-B., Pethig, R. and Jones, T.B. (1992) J. Phys. D Appl. Phys. 25, 881–888.

[13] Gascoyne, P.R.C., Pethig, R., Burt, J.P.H. and Becker, F.F. (1993) Biochim. Biophys. Acta 1149, 119–126.

[14] Gascoyne, P.R.C. and Becker, F.F. (1993) Biochim. Biophys. Acta (submitted).

[15] Gascoyne, P.R.C., Huang, Y., Pethig, R., Vykoukal, J. and Becker, F.F. (1992) Meas. Sci. Technol. 3, 439–445.

[16] Singer, S.J. and Nicolson, G.L. (1972) Science 175, 720–731.

[17] Alberts, B., Bray, D., Lewis, J., Raff, M., Roberts, K. and Watson, J.D. (1983) Molecular Biology of the Cell, Chap. 6, pp. 255–317, Garland, New York.

[18] Irimajiri, A., Asami, K., Ichinowatari, T. and Kinoshita, Y. (1987) Biochim. Biophys. Acta 896, 214–223.

[19] Sukhorukov, V.L., Arnold, W.M. and Zimmermann, U. (1993) J. Membr. Biol. 132, 27–40.

[20] Hu, X., Arnold, W.M. and Zimmermann, U. (1990) Biochim. Biophys. Acta 1021, 191–200.

[21] Lehnert, M.E. and Lodish, H.F. (1988) J. Cell. Biol. 107, 413–426.

[22] Carraway, K.L. and Carraway, C.A.C. (1989) Biochim. Biophys. Acta 988, 147–171.

[23] Leung, M.-F. Sokoloski, J.A. and Sartorelli, A.C. (1992) Cancer Res. 52, 949–954.

[24] CRC Handbook of Chemistry and Physics (1982) CRC Press, pp. D198–D247, Boca Raton, FL.

[25] Sarkadi, B., Attisano, L., Grinstein, S., Buchwald, M. and Rothstein, A. (1984) Biochim. Biophys. Acta 774, 159–168.

[26] Grinstein, S., Clarke, C.A. and Rothstein, A. (1983) J. Gen. Physiol. 82, 619–638.

[27] Grinstein, S., Dupre, A. and Rothstein, A. (1982) J. Gen. Physiol. 79, 849–868.

[28] Huang, Y., Hölzel, R., Pethig., R. and Wang, X.-B. (1992) Phys. Med. Biol. 37, 1499–1517.

[29] Huang, Y. and Pethig, R. (1991) Meas. Sci. Technol. 2, 1142–1146.

[30] Dennis, J.E. and Woods, D.J. (1987) in New Computing Environments: Microcomputers in Large-Scale Computing (Wouk, A., ed.), pp. 116–122, SIAM.

[31] Draper, N.R. and Smith, H. (1980) Applied Regression Analysis, Chap. 10, pp. 472–485.

[32] Schanne, D.F. and Ceretti, E.R.P. (1978) Impedance Measurements in Biological Cells, Wiley & Sons, New York.

[33] Beyer, W.H. (ed.) (1988) CRC Handbook of Tables for Probability and Statistics, pp. 288–289, CRC Press, Boca Raton, FL.

[34] Pauling, L. (1954) General Chemistry, Chap. 16, pp. 347–348, W.H. Freeman, San Francisco.

[35] Fuhr, G., Müller, T., Wagner, A. and Donath, E. (1987) Plant Cell Physiol. 28, 549–555.

[36] Arcangeli, A., Del Bene, M.R., Ricupero, L., Ballerini, L. and Olivotto, M. (1988) Ann. N.Y. Acad. Sci. 551, 242–244.

[37] Vielh, P., Magdelenat, H., Remvikos, Y. and Dutrillaux, B. (1991) in Guides to Clinical Aspiration Biopsy: Flow Cytometry (Vielh, P., ed.), pp. 21–57, Igaku-Shoin, New York.

[38] Gascoyne, P.R.C. and Becker, F.F. (1990) J. Cell. Physiol. 142, 309–315.

[39] Hanai, T., Haydon, D.A. and Taylor, J. (1965) J. Theor. Biol. 9, 278–296.

[40] Fettiplace, R., Andrews, D.M. and Haydon, D.A. (1971) J. Membr. Biol. 5, 277–296.

[41] Benz, R., Fröhlich, O., Läuger, P. and Montal, M. (1975) Biochim. Biophys. Acta 394, 323–334.

[42] Pethig, R. and Kell, D.B. (1987) Phys. Med. Biol., 933–970.

[43] Gennis, R.B. (1989) Biomembranes, pp. 1–35, Springer-Verlag, New York.

[44] Rittmann, L.S., Jelsema, C.L., Schwarz, E.L., Tsiftsoglou, A.S. and Sartorelli, A.C. (1982) J. Cell.. Physiol. 110, 50–55.

[45] Pethig, R. (1979) Dielectric and Electronic Properties of Biological Materials, Chap. 2, pp. 63–67, John Wiley & Sons, Chichester.

[46] Tanka, A. and Ishida, Y. (1973) J. Polym. Sci. Polym. Phys. 11, 1117–1122.

[47] Takashima, S., Asami, K. and Takahashi, Y. (1988) Biophys. J. 54, 995–1000.

[48] Asami, K., Takahashi, Y. and Takashima, S. (1989) Biochim. Biophys. Acta 1010, 49–55.

[49] Felix, H., Haemmerli, G. and Sträuli, P. (1978) Dynamic Morphology of Leukaemia Cells, Springer-Verlag, Berlin.
[50] Marks, P.A. and Rifkind, R.A. (1978) Annu. Rev. Biochem. 47, 419–448.
[51] Friend, C., Scher, W., Holland, J.G. and Sato, T. (1971) Proc. Natl. Acad. Sci. USA 68, 378–382.
[52] Patel, V.P. and Lodish, H.F. (1987) J. Cell. Biol. 105, 3105–3118.
[53] Marks, P.A., Breslow, R., Rifkind, R.A., Ngo, L. and Singh, R. (1989) Proc. Natl. Acad. Sci. USA 86, 6358–6362.
[54] Simon, I., Brown, T.J. and Ginsberg, B.H. (1984) Biochim. Biophys. Acta 803, 39–47.
[55] Simon, I., Brown, T.J. and Ginsberg, B.H. (1987) Biochim. Biophys. Acta 896, 165–172.
[56] Lai, C.-N., Gallick, G.E., Maxwell, S.A., Brinkley, B.R. and Becker, F.F. (1988) J. Cell. Physiol. 134, 445–452.
[57] Fuhr, G. (1985) Über die Rotation dielektrischer Körper in rotierenden Feldern, PhD Dissertation, Humboldt-Universität, Berlin.
[58] Sauer, F.A. and Schlögl, R.W. (1985) Interactions between Electromagnetic Fields and Cells (Chiabrera, A., ed.), pp. 181–202, Plenum Press, New York.
[59] Arnold, W.M. and Zimmermann, U. (1989) Proc. 1st Int. Conf. On Low Cost Exp. on Biophys. (Cairo Univ.) (UNESCO), pp. 1–13.
[60] Glaser, R. and Fuhr, G. (1987) in Mechanistic Approaches to Interactions of Electric and Electromagnetic Fields with Living Systems (Blank, M. and Findl, E., eds.), pp. 271–290, Plenum Press, New York.
[61] Irimajiri, A., Hanai, T. and Inouye, A. (1979) J. Theor. Biol. 78, 251–269.
[62] Marszalek, P., Zielinski, J.J., Fikus, M. and Tsong, T.Y. (1991) Biophys. J. 59, 982–987.